Hindawi
International Journal of Energy Research
Volume 2024, Article ID 9050890, 15 pages
https://doi.org/10.1155/2024/9050890

Research Article

Stabilization of $Li_7La_3Zr_2O_{12}$ Solid Electrolyte through Ga-Based Precipitates and the Ga–Au Surface Layer

Dohun Kim,[1] Minh Hai Nguyen,[1] Seung Hoon Chun,[1] June Jeon,[2] Byung-Kook Kim,[3] and Sangbaek Park[1]

[1]*Department of Materials Science and Engineering, Chungnam National University, Daejeon 34134, Republic of Korea*
[2]*Department of Sociology, Chungnam National University, Daejeon 34134, Republic of Korea*
[3]*Energy Materials Research Center, Korea Institute of Science and Technology (KIST), Seoul 02792, Republic of Korea*

Correspondence should be addressed to Sangbaek Park; sb.park@cnu.ac.kr

Received 1 December 2023; Revised 31 January 2024; Accepted 8 March 2024; Published 28 March 2024

Academic Editor: Hongtao Sun

Garnet-type $Li_7La_3Zr_2O_{12}$ (LLZO) is a promising oxide solid electrolyte with high ionic conductivity and excellent stability toward Li metal. However, the presence of grain boundaries (GBs) causes a decrease in the ionic conductivity and cycling stability of the sintered LLZO. Herein, we promote the Ga precipitation at GBs through excessive doping with Ga/Al/Ta, simultaneously depositing a few nanometers thickness Au layer to form a Ga–Au surface layer. High-temperature sintering of heavily doped LLZO induces Ga precipitation, effectively filling the GB of the pellet. Consequently, the relative density and ionic conductivity are increased. Furthermore, nanoscale Au encounters precipitated Ga and forms a new Ga–Au layer, which reduces the contact resistance. The new layer prevents direct contact between molten Li and Ga-based composites at the GBs, thus enhancing the cycling stability. Therefore, it demonstrates the synergistic effect that the precipitated Ga improves the compactness of the LLZO electrolyte, whereas the Ga–Au layer enhances the cycling stability. It provides a straightforward approach to address the issues originated from GBs and increase the cycling stability of LLZO, thereby contributing to the practical application of all-solid-state batteries.

1. Introduction

Solid-state electrolytes (SSEs) are regarded as alternatives to liquid electrolytes because of their high ionic conductivity, excellent thermal and chemical stability, wide electrochemical window, and superior mechanical properties [1–4]. Such favorable characteristics enable all-solid-state batteries to address the safety and energy density issues of lithium-ion batteries [5]. In this regard, cubic $Li_7La_3Zr_2O_{12}$ (LLZO) is recognized as a promising electrolyte [6–8] because of its excellent electrochemical stability with Li anode [9]. However, LLZO, a polycrystalline ceramic, exhibits elevated grain boundary (GB) resistance, which reduces the ionic conductivity [10, 11]. Additionally, Li dendrite growth is facilitated through the GBs [12], resulting in poor cycling performance [13]. Therefore, reducing the GBs and pores is crucial for the commercialization of LLZO ceramics [14].

Sintering additives have been incorporated into LLZO to effectively achieve compactness in garnet-type electrolytes. Additives such as Li_3PO_4, Li_4GeO_4, and $BaO–B_2O_3–SiO_2–CaO–Al_2O_3$ fill the GB, thereby increasing the density [15–17], preventing the growth of Li dendrites, and enhancing the cycling performance [18, 19]. However, the low Li-ion conductivity of these additives consequently decreases the ionic conductivity of LLZO electrolytes [20, 21]. Meanwhile, LLZO also suffers from poor adhesion with Li metal [22]. For example, molten Li exhibits a high contact angle on the surface of LLZO, and rubbing molten-Li on LLZO induces a structural change in LLZO as Li penetrates through the GBs [23]. Thus, interlayers such as H_3BO_3–HF and Li–Na have been coated on the surface of LLZO to improve its wettability with Li metal [24, 25]. These additives and interlayers complicate the manufacturing process and increase the cost of LLZO solid electrolytes.

The use of Ga, Al, and Ta as a dopant has been previously investigated [26], because Ga and Al can substitute for Li sites in the LLZO lattice and increase the ionic conductivity [27, 28]. Furthermore, Ta substitutes for the Zr site, stabilizing the cubic structure and enhancing ion conductivity at room temperature [29]. Excess Ga is integrated into the structure of Li–Ga compounds ($LiGaO_2$ or Li_x–La_y–Ga_z), positioning itself at the GB, similar to other additives; consequently, the density is increased [30–32]. $LiGaO_2$ creates a new pathway for Li-ion transport between crystal grains, and the ionic conductivity is increased [31]. In addition, the positioning of $LiGaO_2$ at a GB prevents Li_2CO_3 formation and growth upon exposure to air [33]. However, $LiGaO_2$ at the GB releases considerable stress upon encountering molten Li, resulting in substantial defects that adversely affect the cycling performance [34]. Therefore, an alternative method is required for the utilization of Ga precipitation to enhance the ionic conductivity and wettability, while reducing structural deformation and dendrite growth.

In this study, we utilized the heavily doped LLZO with Al, Ga, and Ta to promote the precipitation of Ga from the LLZO lattice. A Ga precipitation mechanism is proposed based on a comprehensive investigation of the electrochemical performance and microstructural changes of the heavily doped LLZO pellets under varying excess Li and Ga contents. The heavily doped Ga in the lattice is replaced with Li atoms at high sintering temperatures, resulting in Ga precipitation between the LLZO particles. The physical and electrical connections of the LLZO particles are improved owing to Ga precipitation, which substantially reduces the GB resistance and enhances Li wettability. To mitigate short-circuit pathway formation within Ga-based compounds at GBs upon the attachment of molten Li, we introduced a few nanometers of Au as an interlayer. The precipitated Ga forms an alloy with Au, resulting in a Ga–Au layer that further reduces the charge transfer resistance and prevents a decrease in the cycling performance by inhibiting direct contact between the molten Li and Ga-based compounds. The synergy between Au and Ga can provide a simple and cost-effective approach for obtaining stable and high-performance LLZO solid electrolytes.

2. Experimental Section

2.1. Preparation of Solid Electrolytes. Solid electrolytes were fabricated using Li_2CO_3 (99.99%; KOJUNDO), La_2O_3 (99.9%; KOJUNDO), ZrO_2 (98%; KOJUNDO), Ga_2O_3 (99.99%; KOJUNDO), Al_2O_3 nanoparticles (<50 nm particle size; Sigma-Aldrich), and Ta_2O_5 (99.9%; KOJUNDO) [35]. The raw material compositions were set at different molar ratios based on the excess Li and Ga contents (Table S1). Each raw powder sample was milled with isopropyl alcohol (IPA; 99.5%; Samchun Pure Chemical Co.) in a planetary mill (Pulverisette 7, FRITSCH, Germany) at 250 rpm for 6 h. After drying, the milled powder was calcined in a box furnace (BF1000-06, MiR, Korea) at 900°C for 6 h. The calcined powder was then pulverized in a planetary mill at 200 rpm for 2 h that is the optimized densification of our LLZO pellets (Figure S1). A polyvinyl alcohol (PVA; Sigma-Aldrich) binder was prepared by stirring PVA in deionized (DI) water (weight ratio 10 : 90) for 24 h. Subsequently, 120 μL of the PVA binder was mixed with 1.8 g of LLZO powder in a mortar in order to increase the pellet density (Figure S2). The resulting mixture was placed in a mold with a diameter of 20 mm and subjected to a pressure of 62 MPa for 10 min to obtain pellets. The compressed pellets, along with the mother powder, were sintered in an MgO crucible at 1250°C for 100 min that is the optimized duration for our LLZO pellets (Figure S3). Finally, the sintered pellets were polished with SiC paper in the order of 220, 400, 1000, 2000, and 5000 grits (Figure S4).

2.2. Characterization. All the powder and pellet samples were subjected to X-ray diffraction (XRD) analysis (D8 ADVANCE, Bruker, Karlsruhe, Germany). The specimens were analyzed using Cu Kα1 radiation within the 2θ range of 10°–80°, at a scanning speed of 1° min^{-1}. The DIFFRAC.EVA computer program (Bruker, Karlsruhe, Germany) was used for crystal phase identification and analysis. The Raman spectroscopy (LabRAM HR-800, Horiba, Kyoto, Japan) was employed as an additional method for the crystal phase analysis of the pellet samples. The morphological characteristics of the samples were analyzed using field emission scanning electron microscopy (FE-SEM; SU-7000, Hitachi, Tokyo, Japan). The elemental distribution of the samples was analyzed using energy dispersive spectroscopy (EDS; Ultim Max 65, Oxford Instruments, Wellington Square, UK). To evaluate the ionic conductivity, the pellet samples were subjected to impedance measurements in the range of 32 MHz to 1 Hz using electrochemical impedance spectroscopy (EIS; Solartron 1260A, Solartron Analytical, Kingston upon Thames, UK). The pellet densities were determined using Archimedes' method with DI water. The Au coating was deposited on a clean, flat pellet surface using an ion sputter coater (SCD 005, Bal-Tec, Milton, NY, USA) at 20 mA for various deposition durations, where the deposition rate is around 0.2 nm/s. The Au-coated pellet was placed in an Ar-filled glove box for 1 h and subsequently heated at 300°C for 15 min. Molten Li was attached at 300°C to assemble the Li|Au|LLZO|Au|Li symmetric structure in a CR2032 cell. Symmetric cells were tested conducted using cyclers (CT-4008T, SinoproMRX, China). X-ray photoelectron spectroscopy (XPS; Nexsa G2, Thermo Fisher Scientific, Massachusetts, USA) was used to analyze the binding forces between the metal atoms, and the binding energy for each element was calculated.

3. Result and Discussion

3.1. Effect of Excess Li. The effect of excess Li stoichiometry was investigated in heavily doped LLZO pellets containing Al, Ga, and Ta dopants by varying the excess Li content with ratios of 1.0, 1.03, 1.1, 1.13, 1.16, and 1.2 ($Li_{7x-0.966}Al_{0.172}Ga_{0.144}La_3Zr_{1.982}Ta_{0.018}O_{12}$, x = 1.0–1.2). After sintering, all pellets exhibited a diameter shrinkage of <85% (Figure S5). Figure 1(a) presents the XRD patterns of the sintered LLZO pellets with excess Li in the range of 1.0–1.2. Secondary peaks are detected in the LLZO pellets with an

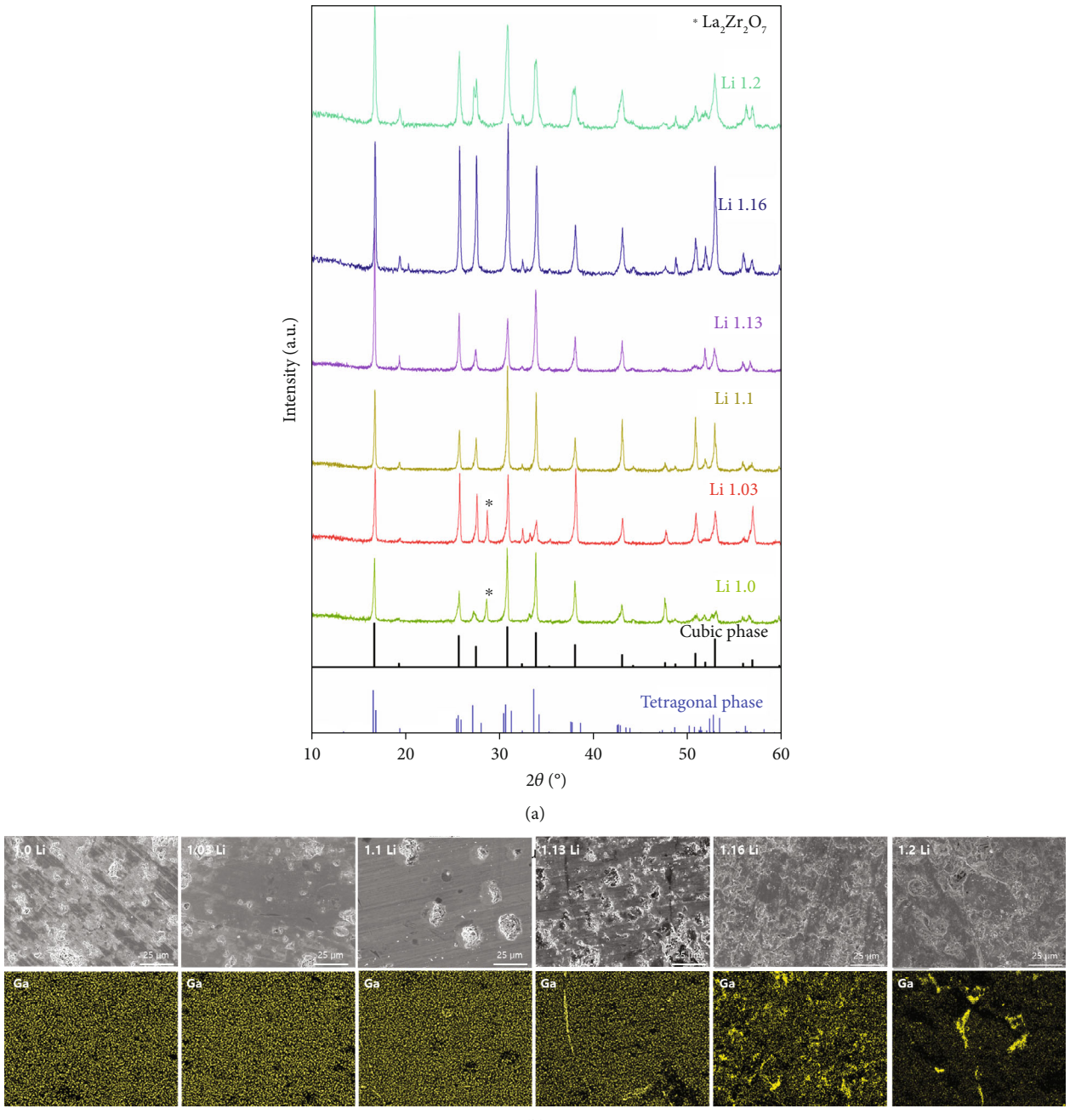

Figure 1: Continued.

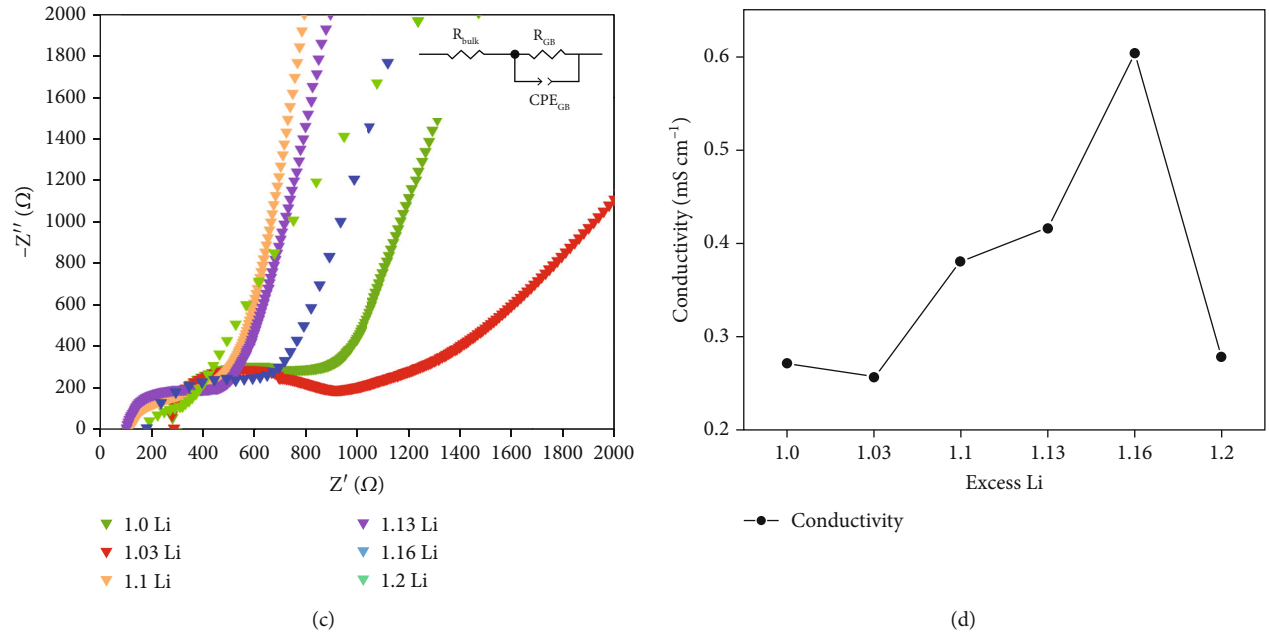

FIGURE 1: Comparison of crystal structure, morphology, and electrochemical properties of $Li_7La_3Zr_2O_{12}$ pellets with excess Li contents of 1.0, 1.03, 1.1, 1.13, 1.16, and 1.2: (a) XRD patterns for sintered $Li_7La_3Zr_2O_{12}$ pellets with varying excess Li contents ranging from 1.0 to 1.2; (b) EDS mapping of Ga based on the top view of the pellet. Scale bar indicates 25 μm; (c) the Nyquist plots and (d) the corresponding ionic conductivities of $Li_7La_3Zr_2O_{12}$ pellets with different excess Li contents.

excess Li of 1.03, as well as in those without excess Li (1.0). As the Li content is increased to 1.1 or 1.13, the secondary peaks diminish, while the tetragonal phase remains, as evidenced by the asymmetric XRD peaks. Samples with an excess Li content of 1.16 exhibit a more pronounced cubic phase than the other samples. The Raman analysis also confirms the successful formation of the cubic phase, with no observable tetragonal phase or Li_2CO_3 (Figure S6) [36, 37]. Above an excess Li content of 1.2, the tetragonal phase reappears. Therefore, the optimal content of excess Li is 1.16 in heavily doped LLZO pellets; this value surpasses 10 wt% excess Li that was used to compensate Li loss in previous multidoped LLZO samples during high-temperature sintering, where the contents of Li vacancy are smaller (e.g., $Li_{6.25}Al_{0.25}La_3Zr_2O_{12}$) than heavily doped LLZO [38–40]. The utilization of excess Li promotes the precipitation of Ga dopants, which occupy Li sites within the LLZO crystal structure during sintering. Figure 1(b) and Figure S7 show the EDS mapping of LLZO pellets with different excess Li. Ga atoms are uniformly distributed on the surface of LLZO pellets at an excess Li content of 1.0 to 1.1. When the Li content is increased to 1.13, Ga is more intensively detected at the GBs of the LLZO pellets, indicating that the Ga dopant is precipitated from LLZO during sintering. Moreover, as the content of excess Li further increases (1.16 and 1.2), additional Ga atoms are observed at the GBs, revealing an increase in the Ga precipitation ratio. Thus, Ga precipitation is attributed to the presence of excess Li, which competes with the dopants for the same atomic positions in the LLZO lattice. This suggests that Ga precipitation at the GBs can be controlled by tuning the Li stoichiometry in heavily doped LLZO. The Nyquist plots and corresponding ionic conductivities of the LLZO pellets with different excess Li contents are shown in Figures 1(c) and 1(d), respectively. In the Nyquist plots, the intersections with the x-axis and semicircle represent the bulk and GB resistances of the LLZO pellet, respectively [41, 42]. The ionic conductivities calculated from the bulk and GB resistances obtained from Figure 1(c) are presented in Table S2. Evidently, LLZO pellets with low (1.0 and 1.03) or high (1.2) levels of excess Li present elevated bulk and GB resistances, ascribed to the presence of secondary phases or the tetragonal phase (Figure 1(a)). In contrast, LLZO pellets with a moderate level of excess Li content (1.1, 1.13, and 1.16) demonstrate enhanced ionic conductivities, attributed to the presence of a high ionic-conducting cubic phase. The LLZO pellet with an excess Li content of 1.16 displays a considerably improved ionic conductivity of 0.604 mS cm^{-1}, indicating a remarkable increase of approximately 150% in ionic conductivity compared with that of LLZO pellets featuring a cubic phase. This is because the GB resistance decreases dramatically as the excess Li content increases from 1.1 to 1.16. The bulk and GB resistances and ionic conductivities for different excess Li contents are summarized in Table S2. These observations imply that Ga precipitation resulting from excess Li reduces the GB resistance by filling the pores and GBs between the LLZO grains.

3.2. Effect of Ga Dopant Concentration. To clarify the influence of precipitated Ga on LLZO electrolytes, we evaluated LLZO pellets with a constant Li excess while varying the Ga dopant content: 0, 0.070, 0.107, 0.142, and 0.178. All pellets were successfully sintered, with a diameter shrinkage of

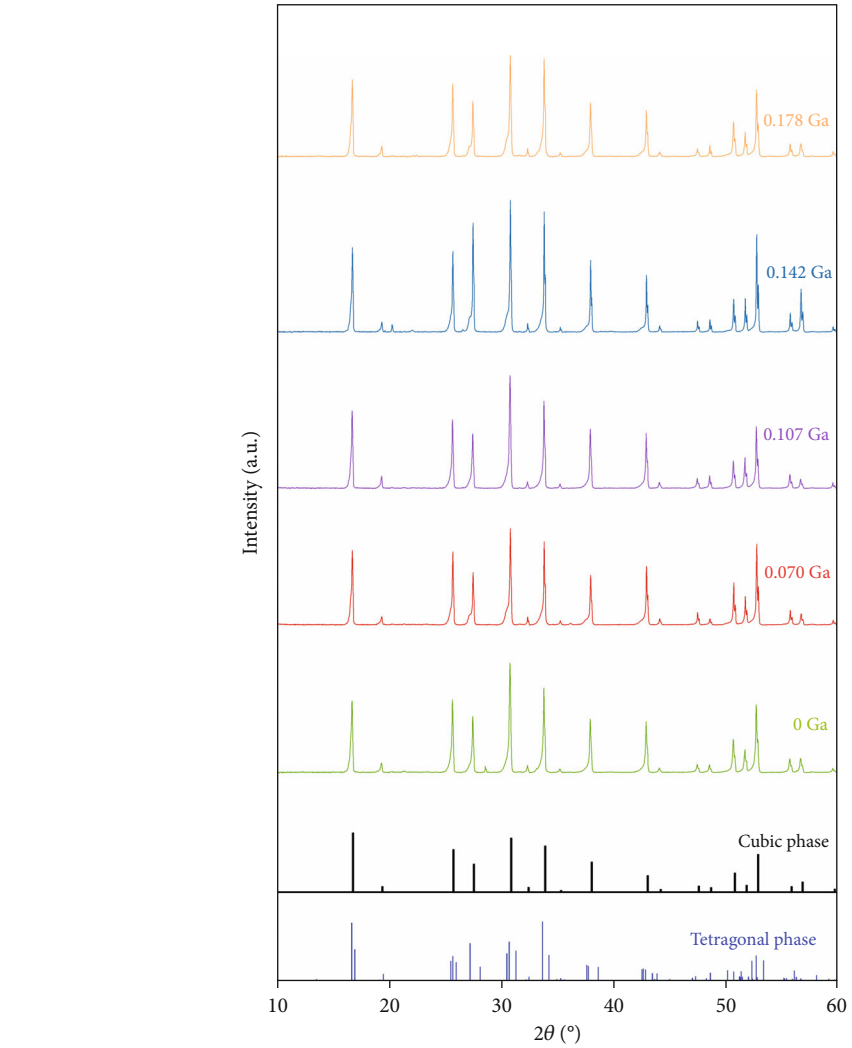

(a)

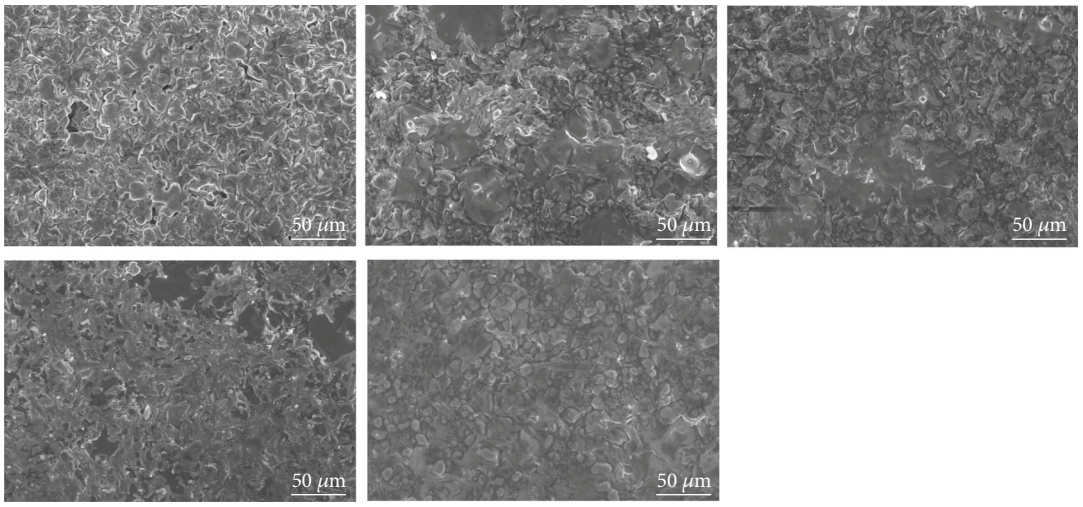

(b)

Figure 2: Continued.

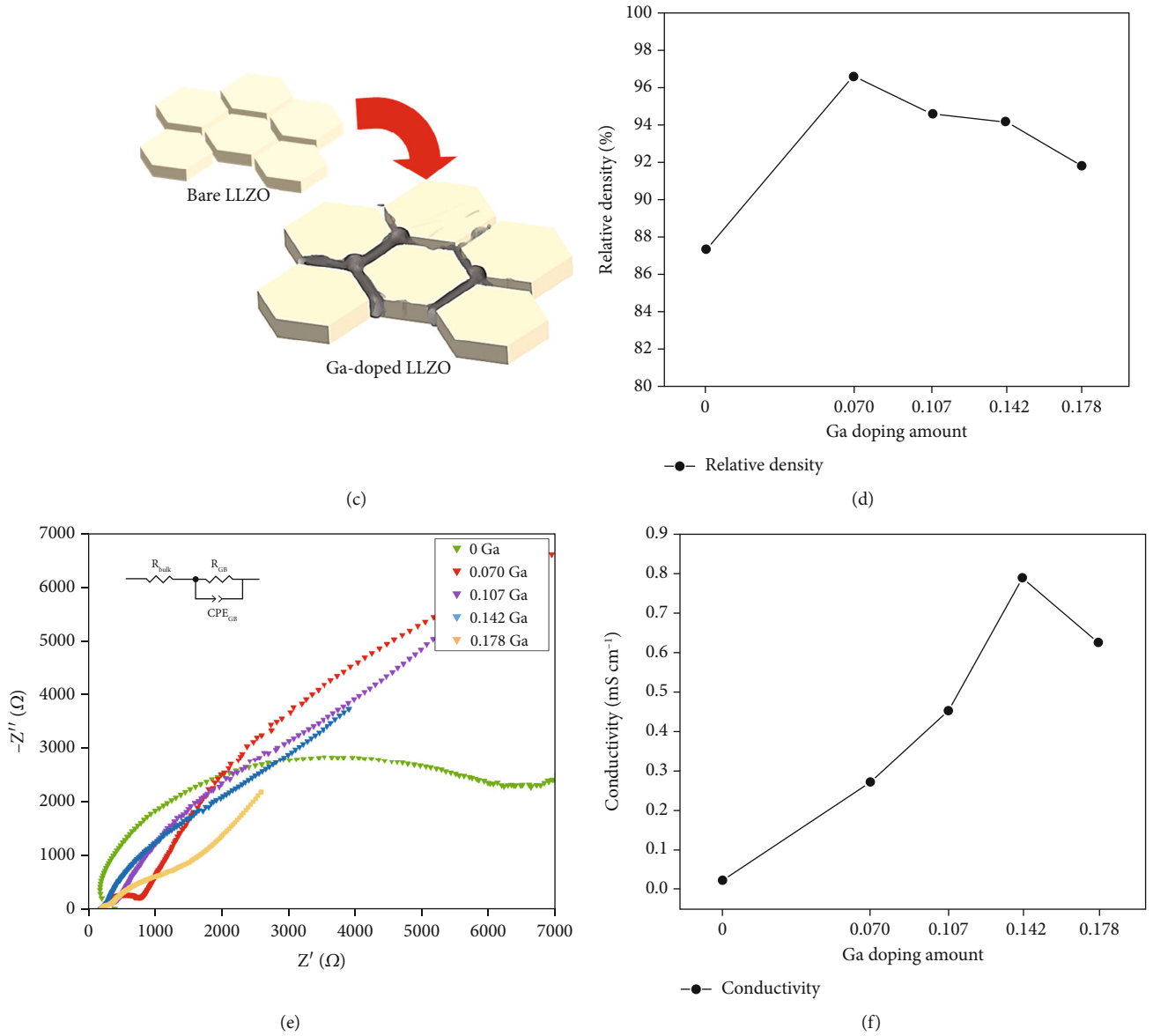

Figure 2: Comparison of crystal structure, morphology, and electrochemical properties of $Li_7La_3Zr_2O_{12}$ pellets with Ga dopant concentrations of 0, 0.070, 0.107, 0.142, and 0.178: (a) XRD patterns of $Li_7La_3Zr_2O_{12}$ electrolytes with the Ga dopant content ranging from 0 to 0.178; (b) top-view SEM images of $Li_7La_3Zr_2O_{12}$ electrolytes with different Ga dopant contents; the $Li_7La_3Zr_2O_{12}$ pellets were polished to achieve a smooth surface; (c) schematic of precipitated Ga in LLZO, facilitating liquid-phase sintering, which accelerates the interparticle bonding in LLZO; (d) relative density of the $Li_7La_3Zr_2O_{12}$ pellets (estimated using Archimedes' method) as a function of Ga dopant content; (e) the Nyquist plots and (f) the corresponding ionic conductivities of $Li_7La_3Zr_2O_{12}$ pellets with increasing Ga content.

approximately 85% (Figure S8). Figure 2(a) shows the XRD patterns of the LLZO electrolytes with the Ga content ranging from 0 to 0.178. The XRD patterns consistently reveal a cubic phase in all LLZO electrolytes because the excess Li content was optimized. Figure 2(b) presents top-view SEM images of the LLZO electrolytes with different Ga dopant contents; the LLZO pellets were polished to achieve a smooth surface. As the Ga content increases from 0 to 0.178, an irregularly shaped liquid-like material gradually fills the GBs and pores between the LLZO particles. This confirms the presence of amorphous compounds, including Ga. Thus, increasing the Ga dopant concentration induces the precipitation of Ga-containing compounds, which are in liquid form at the sintering temperature. As illustrated in Figure 2(c), this implies that the presence of precipitated Ga facilitates liquid-phase sintering, which accelerates interparticle bonding in LLZO [43, 44]. Figure 2(d) presents the relative density of the LLZO pellet, which was estimated using Archimedes' method (Table S3), as a function of the Ga dopant content. The relative density was calculated using Archimedes' formula; the corresponding details are presented in Table S3. Considering LLZO doped solely with Al and Ta, without Ga doping, the relative density is below 90%.

However, the addition of Ga increases the relative density, which reaches 96.6% in the LLZO pellet with a Ga concentration of 0.070. This reveals the role of Ga precipitation in increasing the relative density by filling the GBs and pores. Further increasing the Ga content from 0.107 to 0.178 marginally decreases the relative density of the LLZO pellets. These results indicate maximum localization of the precipitated Ga within the GBs and pores. The Nyquist plots and corresponding ionic conductivities of the LLZO electrolytes with gradually increasing Ga content are presented in Figures 2(e) and 2(f), respectively. The ionic conductivities calculated from the bulk and GB resistances determined from Figure 2(e) are presented in Table S4. The Al- and Ta-doped LLZO sample, without Ga doping, exhibits considerable GB resistance owing to its relatively low density, which results in low ionic conductivity. As the Ga dopant concentration is increased to 0.144, the GB resistance substantially decreases, and the ionic conductivity of LLZO gradually increases. This implies that the amorphous compounds between the LLZO particles improve Li-ion transfer in the GBs. As the Ga content is increased from 0.070 to 0.142, the ionic conductivity increases continuously, even after the relative density of the LLZO pellet reaches a saturated level. This suggests that increasing the Ga ratio within the amorphous compounds may further enhance the Li-ion transport between the LLZO domains, as Ga readily forms alloys with Li. The LLZO pellet with a Ga content of 0.142 exhibits an ionic conductivity of $0.789\,\mathrm{mS\,cm^{-1}}$, which is 36 times higher than that of Al- and Ta-doped LLZO without Ga doping. This is one of the highest values for conventionally sintered LLZO pellets with Ga doping [45]. However, a considerably higher Ga content (0.178) decreases the ionic conductivity of the LLZO pellets. This is attributed to the reduced contact between the LLZO grains, as observed from the decrease in relative density owing to the excessive precipitation of Ga (Figure 2(d)). The bulk and GB resistances and ionic conductivities at different Ga dopant concentrations are summarized in Table S4. Therefore, Ga precipitation enhances the connection between LLZO particles, improving Li-ion migration and enhancing the ionic conductivity of LLZO electrolytes.

3.3. Ga Precipitation Mechanism. To elucidate the Ga precipitation mechanism in the LLZO electrolyte, heavily doped LLZO powder was analyzed after heat treatment at temperatures of 900, 1000, 1100, and 1250°C. In Figure 3(a), EDS mapping images are presented for the LLZO powder with 0.142 Ga doping. At 900°C, all elements, including Ga, are distributed uniformly within the powder. Ga precipitation is not observed, indicating that the dopants are uniformly incorporated into the LLZO lattice. At higher temperatures (1000 to 1250°C), Ga and Al are observed at the interfaces between powders, whereas Ta and La are still uniformly distributed. This indicates the migration of Ga and Al dopants from Li sites within the LLZO lattice to the exterior of the LLZO particles, particularly at temperatures exceeding 1000°C. This phenomenon is related to the formation of a cubic phase with increasing sintering temperature. Figure 3(b) presents the cross-sectional SEM and EDS mapping images for the entire LLZO pellets with Ga concentrations of 0 and 0.142 after sintering at 1250°C. LLZO without Ga doping reveals abundant and wide GB and pores throughout the pellet. In contrast, LLZO with a Ga concentration of 0.142 exhibits Ga precipitation, which fills the GB and pores. The irregular distribution of precipitated Ga in the pellet, compared to the powder, is attributed to the increase in size of LLZO particles during pellet sintering [46]. This indicates that Ga precipitation occurs throughout the pellet and not in localized regions. A schematic of the Ga precipitation mechanism is depicted in Figure 3(c). During the initial stage of sintering, heavily doped Ga occupies the Li sites in the LLZO lattice. Subsequent sintering at temperatures exceeding 1000°C enables Ga to be displaced from the Li sites, resulting in Ga precipitation outside LLZO. Furthermore, the precipitated Ga fills the GBs in the same manner of sintering aids, initiating liquid-phase sintering.

3.4. Effect of Ga Precipitation on the Electrochemical Performance of LLZO Solid Electrolytes. To investigate the impact of Ga precipitation on the electrochemical performance of the LLZO solid electrolytes, symmetric cells were fabricated using LLZO pellets with Ga concentrations of 0 and 0.142 (denoted as Ga-0-LLZO and Ga-0.142-LLZO, respectively). Figure 4(a) shows photographs of an LLZO pellet after the application of molten Li at 300°C. For the LLZO pellet without Ga doping, nonadherence of molten Li is observed, confirming the inadequate Li wettability. In contrast, Ga-0.142-LLZO exhibits improved Li wettability, suggesting that Ga precipitation is beneficial for Li wettability. The following reactions may occur at the interface between the molten Li and the LLZO pellet surface [47]:

(1) $Ga_2O_3 + 6\,Li \longrightarrow 2Ga + 3Li_2O$

(2) $Ga + xLi \longrightarrow Li_xGa$

Following this reaction, the precipitated Ga on the GB reacts with Li to form a Ga–Li alloy, promoting the effective adhesion of molten Li to the LLZO pellet. Figure 4(b) shows the Nyquist plots of the symmetric cells in the presence or absence of Ga precipitation. Both EIS results exhibit two semicircles corresponding to GB resistance and charge transfer resistance [48, 49]. Particularly, Ga precipitation markedly decreases the GB resistance from 3591 to 195.4 Ω and the charge transfer resistance from 1227 to 68.01 Ω. This reveals the contribution of Ga precipitation to the interfacial compatibility with Li in addition to the interconnection between the LLZO particles. Figure S9 displays the galvanostatic cycling performance of LLZO symmetric cells without and with Ga doping at a current density of $0.1\,\mathrm{mA\,cm^{-2}}$ at room temperature. The Li/Ga-0-LLZO/Li cell presented a high voltage (3.2 V) within the first few minutes of applying the current. Subsequently, the voltage dropped to 0.04 V, indicating a short circuit. This was attributed to the formation of Li dendrites through the GBs of the solid electrolyte pellet [50]. In contrast, the Li|Ga-0.142-LLZO|Li cell was stably operated for 7 h, but the subsequent voltage declined because of a short circuit.

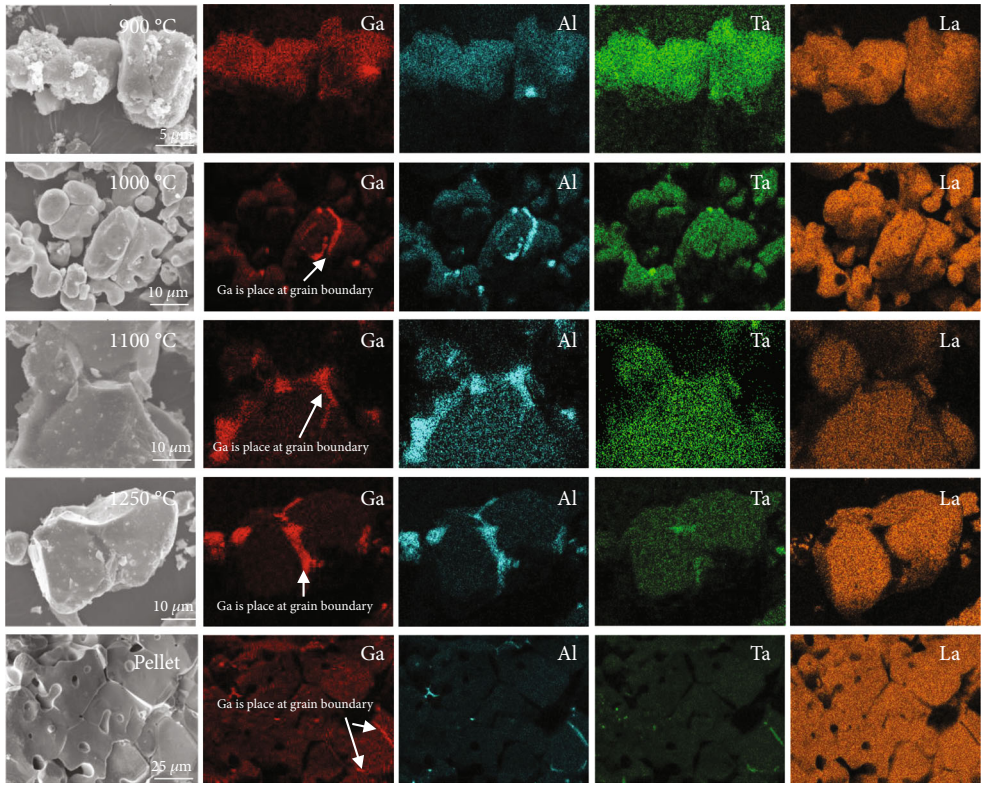

(a)

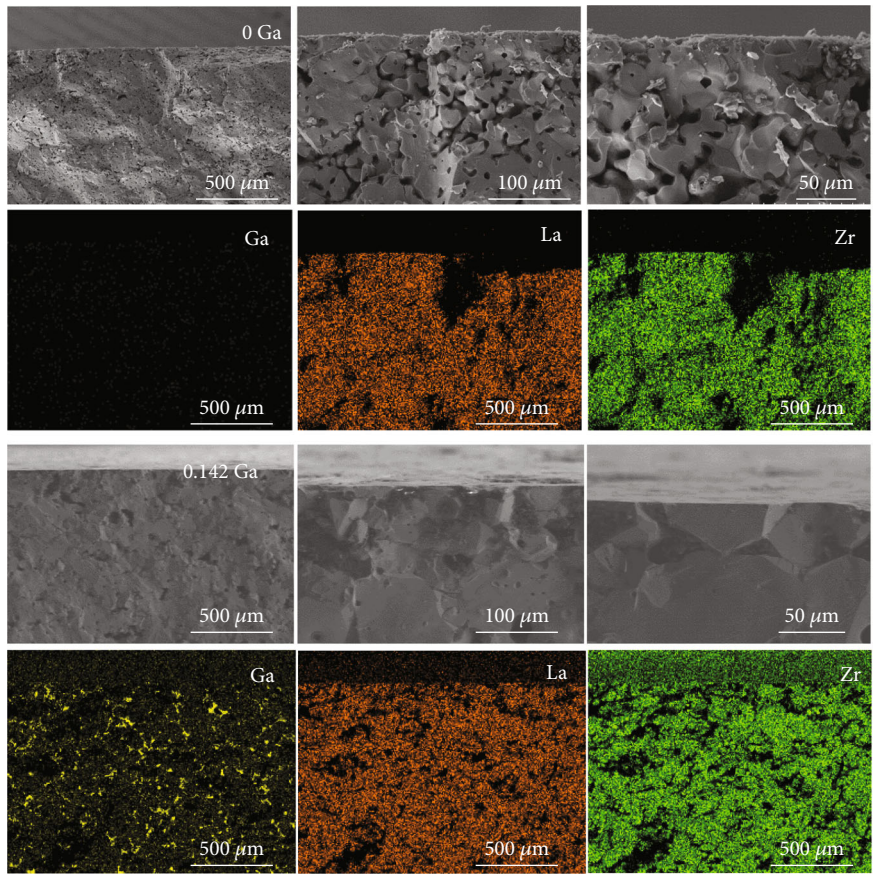

(b)

Figure 3: Continued.

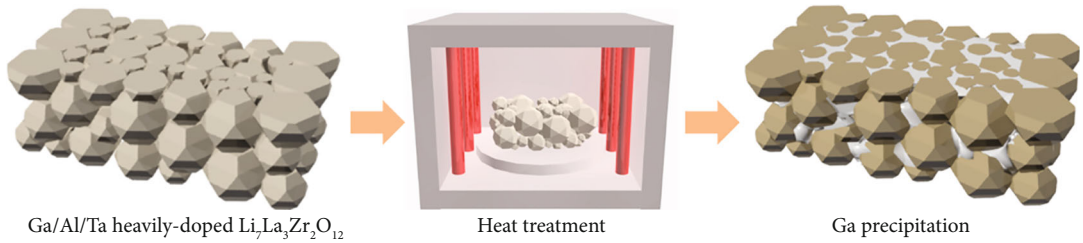

(c)

FIGURE 3: Mechanism of precipitation in Ga/Al/Ta-doped $Li_7La_3Zr_2O_{12}$ electrolyte: (a) EDS mapping images for the $Li_7La_3Zr_2O_{12}$ powder with 0.142 Ga doping, annealed at temperatures of 900, 1000, 1100, and 1250°C; (b) cross-sectional SEM and EDS mapping images for the entire $Li_7La_3Zr_2O_{12}$ pellets with Ga concentrations of 0 and 0.142 after sintering at 1250°C; (c) schematic of the Ga precipitation mechanism.

Therefore, the Li dendrites still grow into GBs filled with Ga-containing compounds. This is ascribed to the reactions of Ga-containing compounds with Li, resulting in crack propagation in the LLZO solid electrolyte during cycling [31]. To mitigate this phenomenon, we deposited an extremely thin Au layer on the LLZO surface before attaching the Li foil. Despite the Au coating, the Ga-0-LLZO symmetric cell exhibited an elevated interface resistance, recorded a high voltage (0.7 V), and experienced a short circuit before completing one cycle (inset of Figure 4(c)). In contrast, the Ga-0.142-LLZO cell exhibited a low interfacial resistance owing to Ga precipitation, with a voltage of 0.087 V. This value is slightly higher than that of Ga-0.142-LLZO without the Au coating, implying that Au acts as a blocking layer [51]. Stable charging and discharging were observed over 200 cycles for 200 h at room temperature in the Li|Au|Ga-0.142-LLZO|Au|Li cell. Therefore, the Au interlayer prevents the decline in cycling stability caused by the precipitated Ga. This demonstrates the synergistic effect of Au and Ga in LLZO, owing to their compatibility.

3.5. Synergistic Effect of Ga–Au Layer. To reveal the synergistic effect of Ga and Au on the Li–LLZO electrolyte interface, surface analysis was conducted by coating Au on the Ga-0.142-LLZO pellet. As shown in Figure 5(a) and Figure S10, the surface color changes from light yellow to dark gray after 1 h of Au coating. This phenomenon occurs as the coated Au encounters Ga, slowly forming an alloy at room temperature [52], as shown in Figure 5(b). Figure 5(c) shows the XRD patterns of the Au-coated LLZO pellets with Ga concentrations of 0 and 0.142. The $AuGa_2$ XRD peak is observed for the Au-coated Ga-0.142-LLZO sample. The $Al_{1.83}Au$ peak is observed in Au-coated Ga-0-LLZO, but not in Au-coated Ga-0.142-LLZO. This implies that Li-Ga-O, with a relatively lower eutectic point than Li-Al-O, exhibits a dominant effect on conductivity enhancement of LLZO doped with both Ga and Al. Figure 5(d) shows the XPS spectrum of Au 4f in Ga-0.142-LLZO. The spectrum of Au $4f^{7/2}$ and Au $4f^{5/2}$ is deconvoluted into two peaks. The first peak has binding energies of 83.4 and 87.1 eV, attributed to metallic gold [53–55]. The second peak is ascribed to the Au–Ga alloy, with binding energies of 84.8 and 89.8 eV [56]. Thus, the surface of the LLZO pellet features the $AuGa_2$ alloy that is formed by the combination of sputtered Au and precipitated Ga. The depth profile analysis results for the Au-coated Ga-0.142-LLZO pellet are depicted in Figures 5(e) and 5(f) and Figure S11. The layer is classified into three parts along the depth: the Au layer, the $AuGa_2$ layer, and the LLZO surface. The Au atomic percentage of the Au layer with etching times ranging from 0 to 40 s exceeds 60%, as observed in the $4f^{7/2}$ and $4f^{5/2}$ peaks. For the $AuGa_2$ layer with an etching time ranging from 40 to 80 s, both Au and Ga exhibit similar atomic percentages, and the Au–Ga peak is observed. Furthermore, beyond an etching time of 80 s, the area corresponding to the LLZO pellet surface is analyzed. This reveals that the Au–Ga layer between Au and LLZO enhances the adhesion strength. Coating Au on garnet-type LLZO is known to facilitate a uniform current distribution on the surface, preventing the formation of Li dendrites [13, 57]. This can also be observed in the Nyquist plot, depending on the presence or absence of the Au coating on the Ga-0-LLZO pellet (Figure S12 and Table S5). The interface resistance is markedly decreased from 12,530 to 1,227 Ω when the pellet is coated with Au. The Ga-precipitated LLZO symmetric cell exhibits an extremely low interface resistance of 68 Ω. This signifies an improvement through both the Li–Au and Au–Ga layers owing to the presence of the Au–Ga alloy. Particularly, a trade-off exists for the Au layer thickness: a thick Au layer blocks Li transport, whereas a thin Au layer is unable to prevent Li dendrite growth. Increasing the Au-coating time from 0 to 20 s does not considerably alter the interface resistance; however, the resistance is doubled at 120 s (Figure S13 and Table S6). Stable galvanostatic cycling is observed with the 120 s Au coating, but the measured voltage is high (0.62 V), indicating a decrease in the electrochemical performance (Figure S14). Additionally, the surface of the LLZO pellet needs to be polished to adjust the surface roughness. A rough surface results in an elevated operating voltage exceeding 1 V for both 20 and 120 s of Au coating at an initial cycle (Figure S15). Polishing to achieve a smooth surface with a roughness of 57.8 nm stabilizes the initial operating voltage (Figure S16 and Figure 4(c)). This implies that a dense and thin Au layer on the smooth pellet surface is necessary to improve both the surface compatibility and stability, which can be

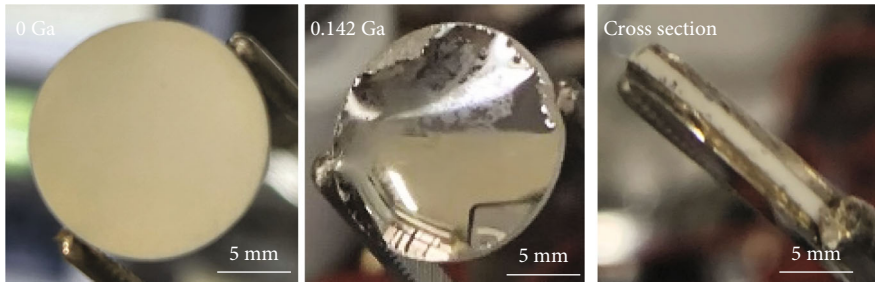

(a)

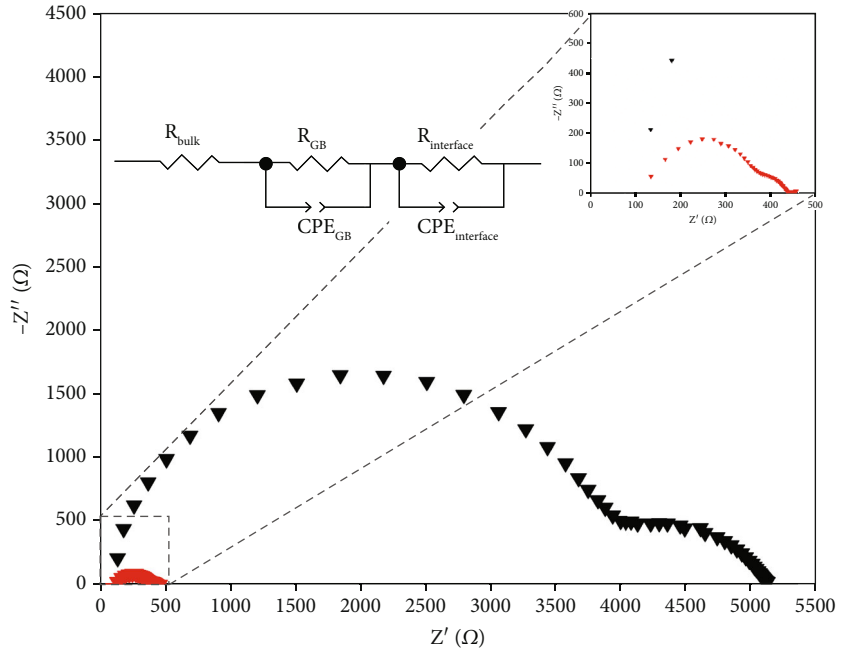

(b)

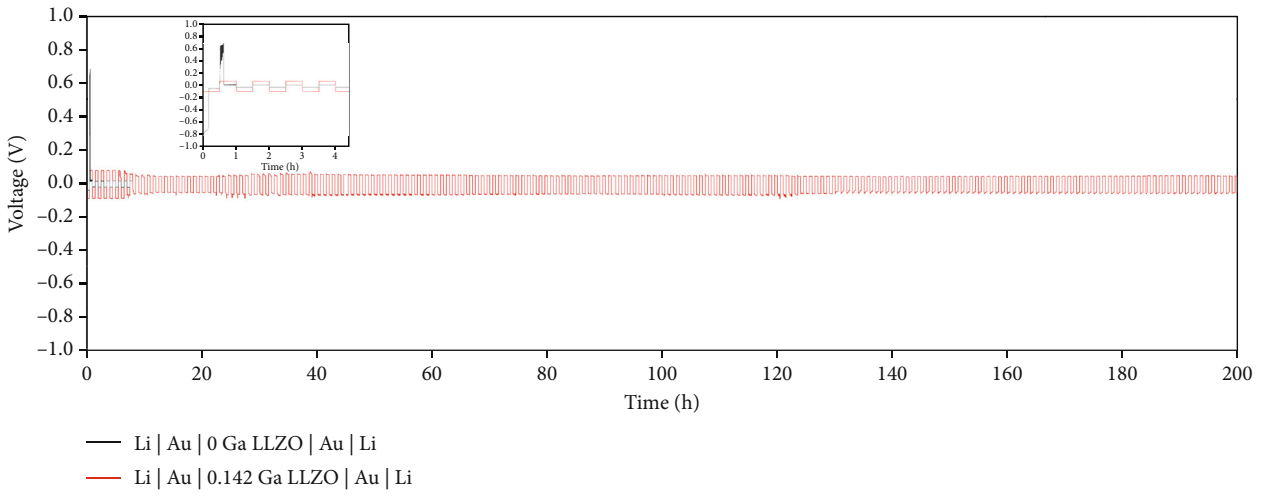

(c)

Figure 4: Performance of symmetric cells with Ga precipitation in $Li_7La_3Zr_2O_{12}$ electrolyte: (a) photographs of a $Li_7La_3Zr_2O_{12}$ pellet after the application of molten Li at 300°C; (b) the Nyquist plots of the symmetric cells according to the presence or absence of Ga precipitation; (c) galvanostatic cycling performance of Li/Au/LLZO/Au/Li symmetric cells without and with Ga doping at a current density of 0.1 mA cm^{-2} at room temperature.

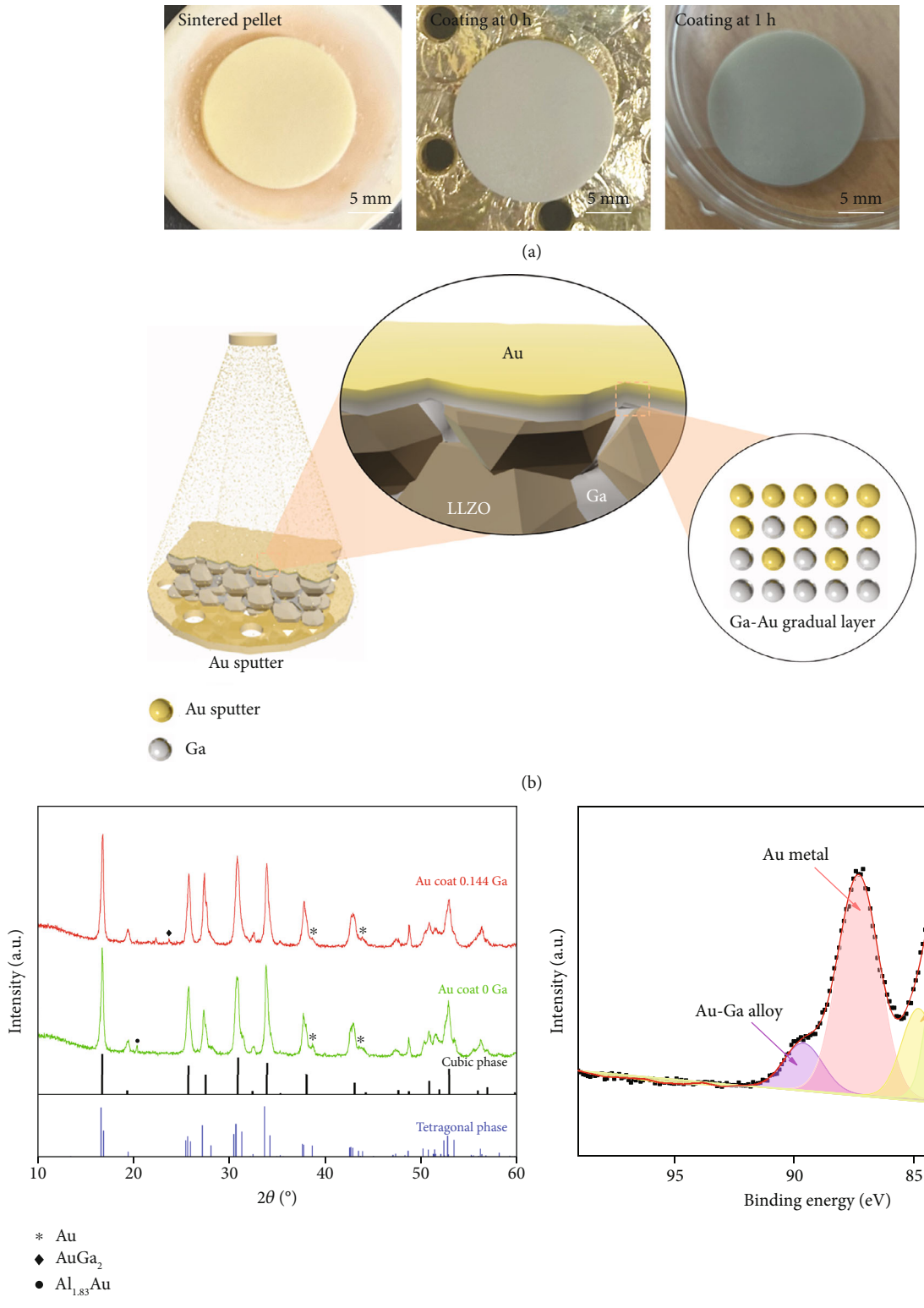

Figure 5: Continued.

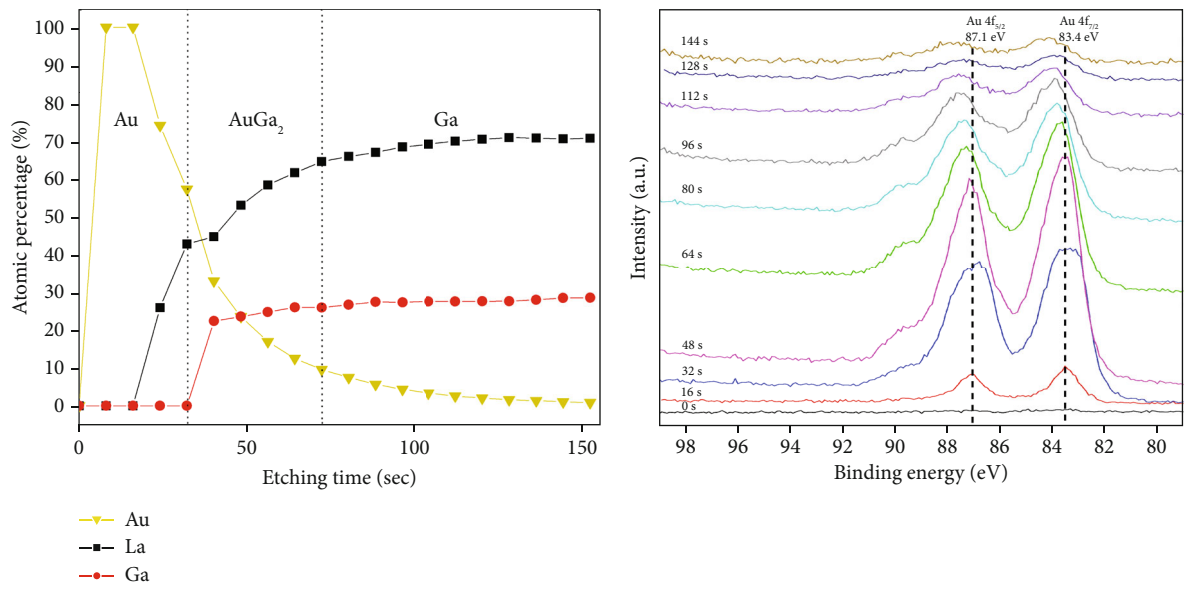

FIGURE 5: Mechanism of Ga–Au interlayer formation on the $Li_7La_3Zr_2O_{12}$ pellet surface: (a) photographs of the change in the surface color from light yellow to dark gray after 1 h of Au coating; (b) process of coated Au encountering Ga to slowly form an alloy at room temperature; (c) XRD patterns of Au-coated $Li_7La_3Zr_2O_{12}$ pellets with a Ga concentration of 0 and 0.142; (d) XPS spectrum of Au 4f for Ga-0.142-LLZO; (e) depth profile analysis and (f) XPS spectrum of etching time results of the Au-coated Ga-0.142-LLZO pellet.

achieved by the Au–Ga alloy on Ga-precipitated LLZO. Therefore, utilizing Ga precipitation for the Ga–Au alloy reduces the contact resistance at the existing Li–Au interface and improves the cycle performance by preventing Li dendrite formation at the Au–LLZO interface.

4. Conclusion

In this study, Ga precipitation in LLZO electrolytes was used to replace conventional additives. In contrast to using additives, precipitation simplified the process through a one-step method. Ga was precipitated through heavy Ga doping, requiring at least 1.1 excess Li. At sintering temperatures exceeding 1000°C, the Ga precipitation mechanism involved Li displacing Ga from the occupied sites. Consequently, the precipitated Ga positioned at the GB successfully achieved a relative density of 96.6% for the LLZO pellet. Furthermore, Ga precipitation improved the connectivity between the LLZO particles, facilitating Li-ion movement and increasing the ionic conductivity of the LLZO electrolyte to 0.789 mS cm^{-1}. Additionally, an Au coating was introduced on the Ga-precipitated LLZO pellet by depositing a thin Au film layer. The deposited Au reacted with the Ga-precipitated layer and formed a Ga–Au alloy layer, which served as a protective buffer, preventing direct contact between the molten Li and precipitated Ga. Thus, Li dendrite growth was inhibited. Finally, the cell exhibited stable cycling for 200 h at room temperature and 0.1 mA cm^{-2}. Furthermore, the introduction of the Ga–Au layer in addition to the conventional Li–Au layer resulted in a remarkably low charge transfer resistance. Therefore, this study introduces a novel strategy for significantly enhancing the microstructure, cycle stability, and interfacial resistance of garnet-type LLZO electrolytes.

Abbreviations

GB: Grain boundary
EDS: Energy dispersive spectroscopy
EIS: Electrochemical impedance spectroscopy
FE-SEM: Field emission scanning electron microscopy
LLZO: $Li_7La_3Zr_2O_{12}$
XPS: X-ray photoelectron spectroscopy
XRD: X-ray diffraction.

Data Availability

The data used to support the findings of this study are available from the corresponding author upon request.

Conflicts of Interest

The authors declare no conflict of interest.

Acknowledgments

This work was supported by the National Research Foundation of Korea (NRF) grant funded by the Korea government (MSIT) (No. 2022R1C1C1006019 and No. RS-2023-00217581). This research was supported by Chungnam National University (2021-2022). This work was supported by BK21 FOUR Program by Chungnam National University Research Grant, 2023.

Supplementary Materials

Table S1: Stoichiometry of $Li_{7x-0.966}Al_{0.172}Ga_{0.144}La_3Zr_{1.982-}Ta_{0.018}O_{12}$ ($x = 1.0, 1.03, 1.1, 1.13, 1.16$) with varying excess Li concentrations. Figure. S1: top-view SEM images of $Li_7La_3Zr_2O_{12}$ solid electrolytes with the powder milling duration of 2 and 12 hours; the $Li_7La_3Zr_2O_{12}$ pellets were polished to achieve a smooth surface. Figure. S2: top-view SEM images of $Li_7La_3Zr_2O_{12}$ solid electrolytes with and without PVA binder; the $Li_7La_3Zr_2O_{12}$ pellets were polished to achieve a smooth surface. Figure. S3: top-view SEM images of $Li_7La_3Zr_2O_{12}$ electrolytes with different sintering time 60 and 100 min; the $Li_7La_3Zr_2O_{12}$ pellets were polished to achieve a smooth surface. Figure. S4: fabrication of $Li_7La_3Zr_2O_{12}$ electrolyte pellets using the top–down approach. Figure. S5: photographs and diameters of sintered $Li_7La_3Zr_2O_{12}$ pellets with excess Li concentrations ranging from 1.0 to 1.2. Figure. S6: the Raman patterns of $Li_7La_3Zr_2O_{12}$ pellet with an excess Li concentration of 1.16 and a dwell time of 2000 ms. Figure. S7: EDS mapping of Al, Ta, and La based on the top view of $Li_7La_3Zr_2O_{12}$ pellets with excess Li contents of 1.0, 1.03, 1.1, 1.13, 1.16, and 1.2. The scale bar indicates 25 μm. Table S2: fitted parameters corresponding to the Nyquist plots and thickness and area of sintered $Li_7La_3Zr_2O_{12}$ pellets with excess Li concentrations ranging from 1.0 to 1.2. Figure. S8: photographs and diameters of sintered $Li_7La_3Zr_2O_{12}$ pellets with Ga dopant concentrations ranging from 0 to 0.178. Table S3: relative density of sintered LLZO pellets with Ga dopant contents ranging from 0 to 0.178. (using Archimedes' method). Table S4: fitted parameters corresponding to the Nyquist plots and thickness and area of sintered $Li_7La_3Zr_2O_{12}$ pellets with Ga dopant concentrations ranging from 0 to 0.178. Figure. S9: galvanostatic cycling performance of Li|LLZO|Li symmetric cells without and with Ga doping at a current density of 0.1 mA cm^{-2} at room temperature. Figure. S10: photo of a smooth surface of Ga-doped (0.142) $Li_7La_3Zr_2O_{12}$ electrolyte with Au coating for 20 s, taken at 10 min intervals. Figure. S11: XPS spectrum of Au-coated Ga-0.142-LLZO for 20 seconds. XPS spectra showing the etching time results for (a) Ga 2p and (b) La 3d of Au-coated Ga-0.142-LLZO. Figure. S12: the Nyquist plot of Li|Ga-0-LLZO|Li symmetric cell without Ga doping $Li_7La_3Zr_2O_{12}$ pellet. Table S5: fitted parameters corresponding to the Nyquist plots for different configurations: Li|Ga-0-LLZO|Li, Li |Au|Ga-0-LLZO|Au|-Li,Li| Au|Ga-0.142-LLZO|Au|Li. Figure. S13: the Nyquist plots of Li|Au|LLZO|Au|Li symmetric cell with Au-coating times of 0 and 120 s on a finely prepared $Li_7La_3Zr_2O_{12}$ pellet surface. Table S6: fitted parameters corresponding to the Nyquist plots of Au-coating times 0, 20, and 120 s on a finely prepared $Li_7La_3Zr_2O_{12}$ pellet surface. Figure. S14: galvanostatic cycling performance of Li|Au|LLZO|Au|Li symmetric cells with different Au coating 0, 120 s on a finely prepared $Li_7La_3Zr_2O_{12}$ surface at a current density of 0.1 mA cm^{-2} at room temperature. Figure. S15: galvanostatic cycling performance of Li|Au|Ga-0.142-LLZO|Au|Li symmetric cells at a current density of 0.1 mA cm^{-2} at room temperature with different Au coating (20 and 120 s) on the surface of LLZO pellets, which were roughly polished using 220 grit sandpaper. Figure. S16: AFM image of sintered $Li_7La_3Zr_2O_{12}$ solid electrolyte with a smooth surface achieved by polishing with 5000 grit sandpaper. *(Supplementary Materials)*

References

[1] C. Wang, K. Fu, S. P. Kammampata et al., "Garnet-type solid-state electrolytes: materials, interfaces, and batteries," *Chemical Reviews*, vol. 120, no. 10, pp. 4257–4300, 2020.

[2] Y. Zhu, X. He, and Y. Mo, "First principles study on electrochemical and chemical stability of solid electrolyte–electrode interfaces in all-solid-state Li-ion batteries," *Journal of Materials Chemistry A*, vol. 4, no. 9, pp. 3253–3266, 2016.

[3] S. H.-S. Cheng, K.-Q. He, Y. Liu et al., "Electrochemical performance of all-solid-state lithium batteries using inorganic lithium garnets particulate reinforced PEO/$LiClO_4$ electrolyte," *Electrochimica Acta*, vol. 253, pp. 430–438, 2017.

[4] R. Chen, Q. Li, X. Yu, L. Chen, and H. Li, "Approaching practically accessible solid-state batteries: stability issues related to solid electrolytes and interfaces," *Chemical Reviews*, vol. 120, no. 14, pp. 6820–6877, 2020.

[5] Q. Zhao, S. Stalin, C.-Z. Zhao, and L. A. Archer, "Designing solid-state electrolytes for safe, energy-dense batteries," *Nature Reviews Materials*, vol. 5, no. 3, pp. 229–252, 2020.

[6] K. V. Kravchyk, D. T. Karabay, and M. V. Kovalenko, "On the feasibility of all-solid-state batteries with LLZO as a single electrolyte," *Scientific Reports*, vol. 12, no. 1, p. 1177, 2022.

[7] V. Thangadurai, S. Narayanan, and D. Pinzaru, "Garnet-type solid-state fast Li ion conductors for Li batteries: critical review," *Chemical Society Reviews*, vol. 43, no. 13, pp. 4714–4727, 2014.

[8] S. Yu, R. D. Schmidt, R. Garcia-Mendez et al., "Elastic properties of the solid electrolyte $Li_7La_3Zr_2O_{12}$ (LLZO)," *Chemistry of Materials*, vol. 28, no. 1, pp. 197–206, 2016.

[9] X. Ke, Y. Wang, L. Dai, and C. Yuan, "Cell failures of all-solid-state lithium metal batteries with inorganic solid electrolytes: lithium dendrites," *Energy Storage Materials*, vol. 33, pp. 309–328, 2020.

[10] Y. Li, Z. Wang, Y. Cao et al., "W-doped $Li_7La_3Zr_2O_{12}$ ceramic electrolytes for solid state Li-ion batteries," *Electrochimica Acta*, vol. 180, pp. 37–42, 2015.

[11] K. H. Kim, T. Hirayama, C. A. J. Fisher et al., "Characterization of grain-boundary phases in $Li_7La_3Zr_2O_{12}$ solid electrolytes," *Materials Characterization*, vol. 91, pp. 101–106, 2014.

[12] S. Yu and D. J. Siegel, "Grain boundary contributions to Li-ion transport in the solid electrolyte $Li_7La_3Zr_2O_{12}$ (LLZO)," *Chemistry of Materials*, vol. 29, no. 22, pp. 9639–9647, 2017.

[13] C.-L. Tsai, V. Roddatis, C. V. Chandran et al., "$Li_7La_3Zr_2O_{12}$Interface modification for Li dendrite prevention," *ACS Applied Materials & Interfaces*, vol. 8, no. 16, pp. 10617–10626, 2016.

[14] X. Huang, J. Tang, Y. Zhou et al., "Developing preparation craft platform for solid electrolytes containing volatile components: experimental study of competition between lithium loss and densification in $Li_7La_3Zr_2O_{12}$," *ACS Applied Materials & Interfaces*, vol. 14, no. 29, pp. 33340–33354, 2022.

[15] C. Wang, Z.-G. Liu, P.-P. Lin et al., "A novel promotion strategy for microstructure and electrical performance of garnet electrolytes via Li_4GeO_4 additive," *Ceramics International*, vol. 49, no. 12, pp. 19905–19915, 2023.

[16] B. Xu, W. Li, H. Duan et al., "Li_3PO_4-added garnet-type $Li_{6.5}La_3Zr_{1.5}Ta_{0.5}O_{12}$ for Li-dendrite suppression," *Journal of Power Sources*, vol. 354, pp. 68–73, 2017.

[17] N. C. Rosero-Navarro, T. Yamashita, A. Miura, M. Higuchi, and K. Tadanaga, "Effect of sintering additives on relative density and Li-ion conductivity of Nb-doped $Li_7La_3ZrO_{12}$ solid electrolyte," *Journal of the American Ceramic Society*, vol. 100, no. 1, pp. 276–285, 2017.

[18] W. Zhang and C. Sun, "Effects of CuO on the microstructure and electrochemical properties of garnet-type $Li_{6.3}La_3Zr_{1.65}W_{0.35}O_{12}$ solid electrolyte," *Journal of Physics and Chemistry of Solids*, vol. 135, 2019.

[19] H. Xie, C. Li, W. H. Kan et al., "Consolidating the grain boundary of the garnet electrolyte LLZTO with Li_3BO_3 for high-performance $LiNi_{0.8}Co_{0.1}Mn_{0.1}O_2$/$LiFePO_4$hybrid solid batteries," *Journal of Materials Chemistry A*, vol. 7, no. 36, pp. 20633–20639, 2019.

[20] S. V. Pershina, E. A. Il'ina, and O. G. Reznitskikh, "Phase composition, density, and ionic conductivity of the $Li_7La_3Zr_2O_{12}$-based composites with LiPO3Glass addition," *Inorganic Chemistry*, vol. 56, no. 16, pp. 9880–9891, 2017.

[21] B. Wang, B. C. Chakoumakos, B. C. Sales, B. S. Kwak, and J. B. Bates, "Synthesis, crystal structure, and ionic conductivity of a polycrystalline lithium phosphorus oxynitride with the γ-Li_3PO_4 structure," *Journal of Solid State Chemistry*, vol. 115, no. 2, pp. 313–323, 1995.

[22] W. Ji, B. Luo, Q. Wang et al., "Revealing the influence of surface microstructure on Li wettability and interfacial ionic transportation for garnet-type electrolytes," *Advanced Energy Materials*, vol. 13, no. 21, article 2300165, 2023.

[23] J. Su, X. Huang, Z. Song et al., "Overcoming the abnormal grain growth in Ga-doped $Li_7La_3Zr_2O_{12}$ to enhance the electrochemical stability against Li metal," *Ceramics International*, vol. 45, no. 12, pp. 14991–14996, 2019.

[24] M. Cai, J. Jin, T. Xiu, Z. Song, M. E. Badding, and Z. Wen, "In-situ constructed lithium-salt lithiophilic layer inducing bifunctional interphase for stable LLZO/Li interface," *Energy Storage Materials*, vol. 47, pp. 61–69, 2022.

[25] Y. Zhang, J. Meng, K. Chen, H. Wu, J. Hu, and C. Li, "Garnet-based solid-state lithium fluoride conversion batteries benefiting from eutectic interlayer of superior wettability," *ACS Energy Letters*, vol. 5, no. 4, pp. 1167–1176, 2020.

[26] L.-H. Huang and C.-C. Li, "Liquid metallic Ga as sintering aid to promote the densification of garnet electrolytes for all-solid-state Li-ion batteries," *Journal of Power Sources*, vol. 556, p. 232527, 2023.

[27] R. Jalem, M. J. D. Rushton, W. Manalastas Jr. et al., "Effects of gallium doping in garnet-type Li7La3Zr2O12Solid electrolytes," *Chemistry of Materials*, vol. 27, no. 8, pp. 2821–2831, 2015.

[28] M. Ashuri, M. Golmohammad, A. Soleimany Mehranjani, and M. Faghhi Sani, "Al-doped $Li_7La_3Zr_2O_{12}$ garnet-type solid electrolytes for solid-state Li-ion batteries," *Journal of Materials Science: Materials in Electronics*, vol. 32, no. 5, pp. 6369–6378, 2021.

[29] R. Inada, A. Takeda, Y. Yamazaki, S. Miyake, and V. Thangadurai, "Effect of postannealing on the properties of a Ta-doped $Li_7La_3Zr_2O_{12}$Solid electrolyte degraded by Li dendrite penetration," *ACS Applied Energy Materials*, vol. 3, no. 12, pp. 12517–12524, 2020.

[30] C. Schwab, G. Häuschen, M. Mann et al., "Towards economic processing of high performance garnets – case study on zero Li excess Ga-substituted LLZO," *Journal of Materials Chemistry A*, vol. 11, no. 11, pp. 5670–5680, 2023.

[31] H. El Shinawi and J. Janek, "Stabilization of cubic lithium-stuffed garnets of the type "$Li_7La_3Zr_2O_{12}$" by addition of gallium," *Journal of Power Sources*, vol. 225, pp. 13–19, 2013.

[32] O. Sharifi, M. Golmohammad, M. Soozandeh, and A. S. Mehranjani, "Improved Ga-doped $Li_7La_3Zr_2O_{12}$ garnet-type solid electrolytes for solid-state Li-ion batteries," *Journal of Solid State Electrochemistry*, vol. 27, no. 9, pp. 2433–2444, 2023.

[33] W. Jeong, S. S. Park, J. Yun, H. R. Shin, J. Moon, and J.-W. Lee, "Tailoring grain boundary structures and chemistry of $Li_7La_3Zr_2O_{12}$ solid electrolytes for enhanced air stability," *Energy Storage Materials*, vol. 54, pp. 543–552, 2023.

[34] J. Li, H. Luo, K. Liu et al., "Excellent stability of Ga-doped garnet electrolyte against Li metal AnodeviaEliminating LiGaO2-Precipitates for advanced all-solid-state batteries," *ACS Applied Materials & Interfaces*, vol. 15, no. 5, pp. 7165–7174, 2023.

[35] M. H. Nguyen and S. Park, "Synergetic effect of Li-ion concentration and triple doping on ionic conductivity of $Li_7La_3Zr_2O_{12}$ solid electrolyte," *Nanomaterials*, vol. 12, no. 17, p. 2946, 2022.

[36] F. Tietz, T. Wegener, M. T. Gerhards, M. Giarola, and G. Mariotto, "Synthesis and Raman micro-spectroscopy investigation of $Li_7La_3Zr_2O_{12}$," *Solid State Ionics*, vol. 230, pp. 77–82, 2013.

[37] G. Larraz, A. Orera, and M. L. Sanjuán, "Cubic phases of garnet-type $Li_7La_3Zr_2O_{12}$: the role of hydration," *Journal of Materials Chemistry A*, vol. 1, no. 37, pp. 11419–11428, 2013.

[38] I. N. David, T. Thompson, J. Wolfenstine, J. L. Allen, and J. Sakamoto, "Microstructure and Li-ion conductivity of hot-pressed cubic $Li_7La_3Zr_2O_{12}$," *Journal of the American Ceramic Society*, vol. 98, no. 4, pp. 1209–1214, 2015.

[39] Y. Jin and P. J. McGinn, "$Li_7La_3Zr_2O_{12}$ electrolyte stability in air and fabrication of a Li/$Li_7La_3Zr_2O_{12}$/$Cu_{0.1}V_2O_5$ solid-state battery," *Journal of Power Sources*, vol. 239, pp. 326–331, 2013.

[40] R.-J. Chen, M. Huang, W.-Z. Huang, Y. Shen, Y.-H. Lin, and C.-W. Nan, "Effect of calcining and Al doping on structure and conductivity of $Li_7La_3Zr_2O_{12}$," *Solid State Ionics*, vol. 265, pp. 7–12, 2014.

[41] Y. Meesala, Y.-K. Liao, A. Jena et al., "An efficient multi-doping strategy to enhance Li-ion conductivity in the garnet-type solid electrolyte $Li_7La_3Zr_2O_{12}$," *Journal of Materials Chemistry A*, vol. 7, no. 14, pp. 8589–8601, 2019.

[42] X. Xiang, F. Chen, Q. Shen, L. Zhang, and C. Chen, "Effect of the lithium ion concentration on the lithium ion conductivity of Ga-doped LLZO," *Materials Research Express*, vol. 6, no. 8, article 085546, 2019.

[43] R.-H. Shin, S. I. Son, Y. S. Han et al., "Sintering behavior of garnet-type $Li_7La_3Zr_2O_{12}$-Li_3BO_3 composite solid electrolytes for all-solid-state lithium batteries," *Solid State Ionics*, vol. 301, pp. 10–14, 2017.

[44] Y. Jin and P. J. McGinn, "Al-doped $Li_7La_3Zr_2O_{12}$ synthesized by a polymerized complex method," *Journal of Power Sources*, vol. 196, no. 20, pp. 8683–8687, 2011.

[45] J. Li, J. Zhang, H. Zhai, X. Tang, and G. Tan, "Rapid synthesis of garnet-type $Li_7La_3Zr_2O_{12}$ solid electrolyte with superior electrochemical performance," *Journal of the European Ceramic Society*, vol. 42, no. 4, pp. 1568–1575, 2022.

[46] S. Vema, A. H. Berge, S. Nagendran, and C. P. Grey, "Clarifying the dopant local structure and effect on ionic conductivity

in garnet solid-state electrolytes for lithium-ion batteries," *Chemistry of Materials*, vol. 35, no. 22, pp. 9632–9646, 2023.

[47] J. Liu, W. Guo, H. Guo et al., "A simple and efficient strategy for ameliorating Li/LLZO interfacial contact," *Energy & Fuels*, vol. 36, no. 15, pp. 8500–8505, 2022.

[48] S. Lee, S. Jung, S. Yang et al., "Revisiting the LiPON/Li thin film as a bifunctional interlayer for NASICON solid electrolyte-based lithium metal batteries," *Applied Surface Science*, vol. 586, article 152790, 2022.

[49] H. Koshikawa, S. Matsuda, K. Kamiya et al., "Electrochemical impedance analysis of the Li/Au-$Li_7La_3Zr_2O_{12}$ interface during Li dissolution/deposition cycles: effect of pre-coating $Li_7La_3Zr_2O_{12}$ with Au," *Journal of Electroanalytical Chemistry*, vol. 835, no. 15, pp. 143–149, 2019.

[50] S. Kim, C. Jung, H. Kim et al., "The role of interlayer chemistry in Li-metal growth through a garnet-type solid electrolyte," *Advanced Energy Materials*, vol. 10, no. 12, article 100537, 2020.

[51] P. Barai, A. T. Ngo, B. Narayanan, K. Higa, L. A. Curtiss, and V. Srinivasan, "The role of local inhomogeneities on dendrite growth in LLZO-based solid electrolytes," *Journal of The Electrochemical Society*, vol. 167, no. 10, article 100537, 2020.

[52] R. P. Elliott and F. A. Shunk, "The Au-Ga (gold-gallium) system," *Bulletin of Alloy Phase Diagrams*, vol. 2, no. 3, pp. 356–358, 1981.

[53] İ. A. Kariper, M. O. Çağlayan, and Z. Üstündağ, "Heterogeneous Au/Ru hybrid nanoparticle decorated graphene oxide nanosheet catalyst for the catalytic reduction of nitroaromatics," *Research on Chemical Intermediates*, vol. 45, no. 2, pp. 801–813, 2019.

[54] E. Dilonardo, M. Penza, M. Alvisi et al., "Electrophoretic deposition of Au NPs on CNT networks for sensitive NO_2 detection," *Journal of Sensors and Sensor Systems*, vol. 3, no. 2, pp. 245–252, 2014.

[55] A. Devia, V. Benavides, H. A. Castillo, and J. Quintero, "Effects of the substrate temperature in AuN thin films by means of X-ray diffraction," *AIP Conference Proceedings*, vol. 875, no. 1, pp. 258–261, 2006.

[56] C.-C. Negrila, M. F. Lazarescu, C. Logofatu et al., "XPS analysis of AuGeNi/cleaved GaAs(110) interface," *Journal of Nanomaterials*, vol. 2016, Article ID 7574526, 6 pages, 2016.

[57] L. C. Zhang, J. F. Yang, C. L. Li, Y. X. Gao, X. P. Wang, and Q. F. Fang, "Intragranular growth and evenly distribution mechanism of Li metal in $Li_7La_3Zr_2O_{12}$ electrolyte," *Journal of Power Sources*, vol. 449, no. 15, p. 227610, 2020.